

# Versatile photonic frequency synthetic dimensions using a single Mach-Zehnder-interferometer-assisted device on thin-film lithium niobate

Zhao-An Wang,<sup>1,2,3,\*</sup> Xiao-Dong Zeng,<sup>1,2,3,\*</sup> Yi-Tao Wang,<sup>1,2,3,\*</sup> Jia-Ming Ren,<sup>1,2,3</sup> Chun Ao,<sup>1,2,3</sup>  
Zhi-Peng Li,<sup>1,2,3</sup> Wei Liu,<sup>1,2,3</sup> Nai-Jie Guo,<sup>1,2,3,4</sup> Lin-Ke Xie,<sup>1,2,3</sup> Jun-You Liu,<sup>1,2,3,4</sup> Yu-Hang Ma,<sup>1,2,3</sup>  
Ya-Qi Wu,<sup>1,2,3</sup> Shuang Wang,<sup>1,2,3,4</sup> Jian-Shun Tang,<sup>1,2,3,4,†</sup> Chuan-Feng Li,<sup>1,2,3,4,‡</sup> and Guang-Can Guo<sup>1,2,3,4</sup>

<sup>1</sup>CAS Key Laboratory of Quantum Information, University of Science and Technology of China, Hefei, 230026, China

<sup>2</sup>Anhui Province Key Laboratory of Quantum Network,

University of Science and Technology of China, Hefei, Anhui 230026, China

<sup>3</sup>CAS Center For Excellence in Quantum Information and Quantum Physics,  
University of Science and Technology of China, Hefei, 230026, China

<sup>4</sup>Hefei National Laboratory, University of Science and Technology of China, Hefei 230088, China

(Dated: November 21, 2024)

Investigating physical models with photonic synthetic dimensions has been generating great interest in vast fields of science. The rapid developing thin-film lithium niobate (TFLN) platform, for its numerous advantages including high electro-optic coefficient and scalability, is well compatible with the realization of synthetic dimensions in the frequency together with spatial domain. While coupling resonators with fixed beam splitters is a common experimental approach, it often lacks tunability and limits coupling between adjacent lattices to sites occupying the same frequency domain positions. Here, on the contrary, we conceive the resonator arrays connected by electro-optic tunable Mach-Zehnder interferometers in our configuration instead of fixed beam splitters. By applying bias voltage and RF modulation on the interferometers, our design extends such coupling to long-range scenario and allows for continuous tuning on each coupling strength and synthetic effective magnetic flux. Therefore, our design enriches controllable coupling types that are essential for building programmable lattice networks and significantly increases versatility. As the example, we experimentally fabricate a two-resonator prototype on the TFLN platform, and on this single chip we realize well-known models including tight-binding lattices, topological Hall ladder and Creutz ladder. We directly observe the band structures in the quasi-momentum space and important phenomena such as spin-momentum locking and the Aharonov-Bohm cage effect. These results demonstrate the potential for convenient simulations of more complex models in our configuration.

## Introduction

Creating a controllable artificial system, of which the dynamics highly resembles the one in real space, is a commonly used method to simulate inaccessible, complex and high-dimensional systems. The artificial systems also called synthetic dimensions, are therefore capable to investigate fascinating novel physics in the field of such as solid-state physics [1–4]. In terms of realization, photonic system hold advantages since it has multiple manipulable degrees of freedom including polarization, space, frequency and orbital angular momentum [5–16]. Configuring synthetic dimensions in the form of optical frequency lattices is one of the popular approaches in pioneering works, where optical-fiber-based resonators are mainly exploited [16–22].

Apart from optical fibers, integrated optics holds promise for generating even more complex and programmable lattice networks for its good scalability, stability and reconfigurability. Especially, with broad transparent spectrum, high non-linear and electro-optic coefficients, thin-film lithium niobate (TFLN) provides an ideal platform. The rapid development of high per-

formance devices on such platform including modulated resonators have paved the way for frequency synthetic dimensions [23–31]. As a result, constructing frequency lattices on TFLN has garnered increasing interest recently and several experimental works, such as Ref. [32–36] and our previous work Ref. [37], have been reported.

To extend the dimensions of lattices and interaction in synthetic dimensions, the realization of coherent coupling between resonators is crucial. When two resonators are connected with a passive coupler, adjacent coupling emerges between two lattices (resonators) at the same-frequency lattices points. It allows for the combination of the frequency and spatial dimension for simulating various models and engrossing phenomena, e.g., the Hall ladder, honeycomb lattices, band structures with effective magnetic field, and spin-momentum locking, etc. [18, 31]. Moreover, controllable long-range coupling, such as cross coupling, is crucial for more general models. For example, the historically important model of Creutz ladder [38–41] requires the cross coupling between different-frequency points in different lattices, but still awaits experimental investigation leveraging frequency synthetic dimensions since the lack of sufficiently tunable coupling methods. Therefore, improving the tunability of the coupling modes between resonators is necessary to tune the lattice and realize more physical model.

In this work, we design and fabricate a Mach-Zehnder-

\* These authors contributed equally to this work.

† [tjs@ustc.edu.cn](mailto:tjs@ustc.edu.cn)

‡ [cffi@ustc.edu.cn](mailto:cffi@ustc.edu.cn)

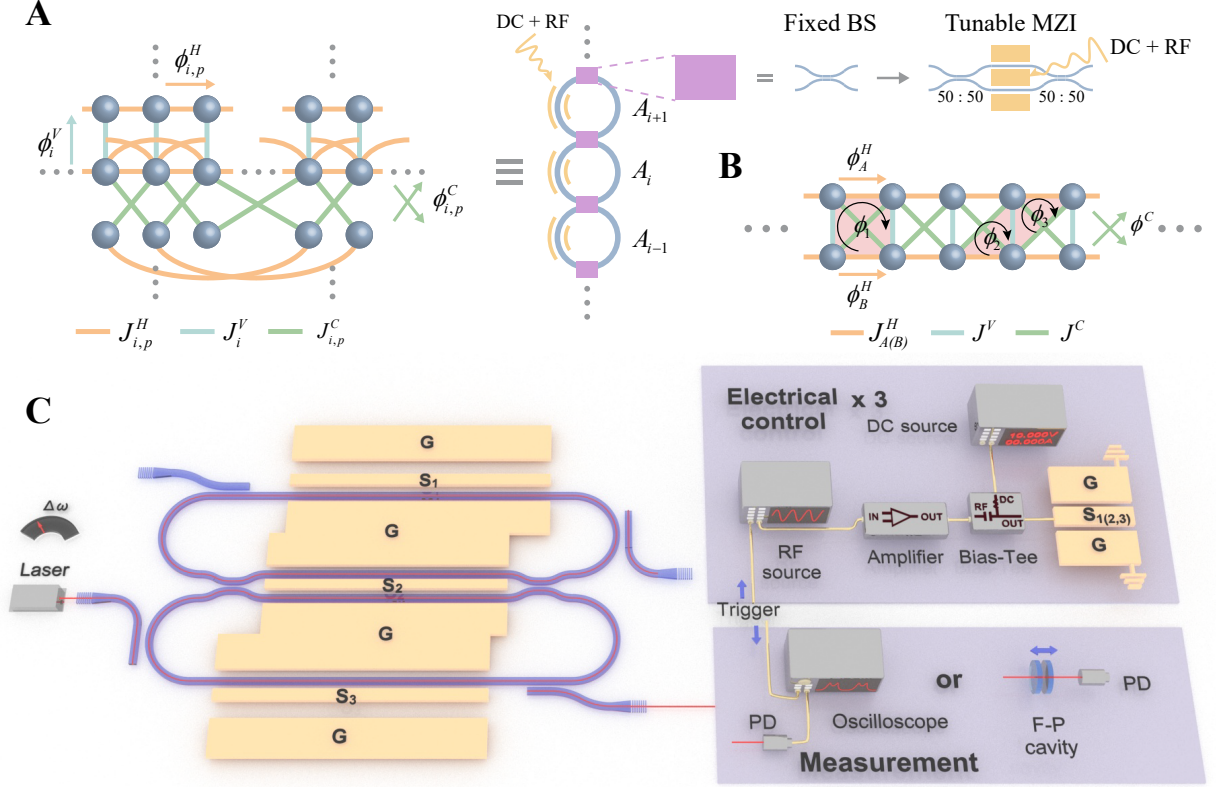


Fig. 1. **Schematic and experimental setup.** (A) Configuration of a lattice network in frequency synthetic dimensions. The lattice network is simulated by a train of modulated resonators. Instead of fixed beam splitters (BS), MZIs tunable by DC and RF signals are used to couple the adjacent resonators (purple boxes). The lattice network consequently contains three types of coupling stemming from local modulation on the resonators (orange), DC (cyan) and RF (green) signals applied on the MZIs, respectively. (B) Schematic of the Creutz ladder. The coupling types are of same definition in A and  $\phi_1$ ,  $\phi_2$  and  $\phi_3$  are the potential gauges. (C) Experimental setup for realizing B with two MZI assisted race-track resonators on TFLN. Three sets of electrical signals consisting of DC and RF parts are applied on three sets of the ground-signal-ground (GSG) arranged electrodes through Bias-Tees to control the two resonators ( $S_1$ ,  $S_3$ ) and the MZI ( $S_2$ ). For detecting band structures, a probe laser with detuning  $\Delta\omega$  is injected to excite the bands. The time- (quasi-momentum-) varying transmittance signal, which is a slice of the band structure, is detected by a photodetector (PD) followed by an oscilloscope triggered by the RF source. For obtaining mode distribution, the measurement part is replaced by scanning a Fabry-Perot (F-P) cavity together with a photodetector.

interferometer (MZI)-assisted double-resonator device on TFLN, and then realize the sufficient regulation of coupling strength and range in synthetic dimensions. By tuning the bias voltage applied on the MZI [42], we are able to arbitrarily tune the coupling strength between two modulated resonators and explore every model mentioned above with this single device. More importantly, by modulating the MZI rather than resonators with RF signals, we further extend the adjacent coupling to cross coupling and long-range coupling, without introducing auxiliary resonators [43, 44]. This enable us to simulate more complex modle like Creutz ladder. We show the experimental observation of band structures of tight-binding lattices, the Hall ladder and the Creutz ladder, as well as topological features including gauge potential and Aharonov-Bohm cage. While maintaining a similar scale and fabrication difficulty to using fixed beam splitters as couplers, our configuration significantly increases the

versatility of devices for realizing frequency synthetic dimensions and broadens the scope of models that can be simulated.

## Theoretical framework

Design of the couplings among the lattice network points is one of the core ingredients of the configuration of physical models, specifically, both the coupled modes and coupling range are required to be tuned appropriately. Towards an ideal versatile and programmable network, a device being capable to cover as many coupling types as possible is on demand. Now we consider a 2D network protocol constituted by a series of identically-adjacently-coupled 1D lattices, which can be simulated by a train of resonators (Fig. 1A), by integrating the frequency and the spatial domain. We can depict the general model with the horizontal, vertical, crossing coupling strengths ( $J_{i,p}^H$ ,  $J_i^V$ ,  $J_{i,p}^C$ ), as well as the corresponding

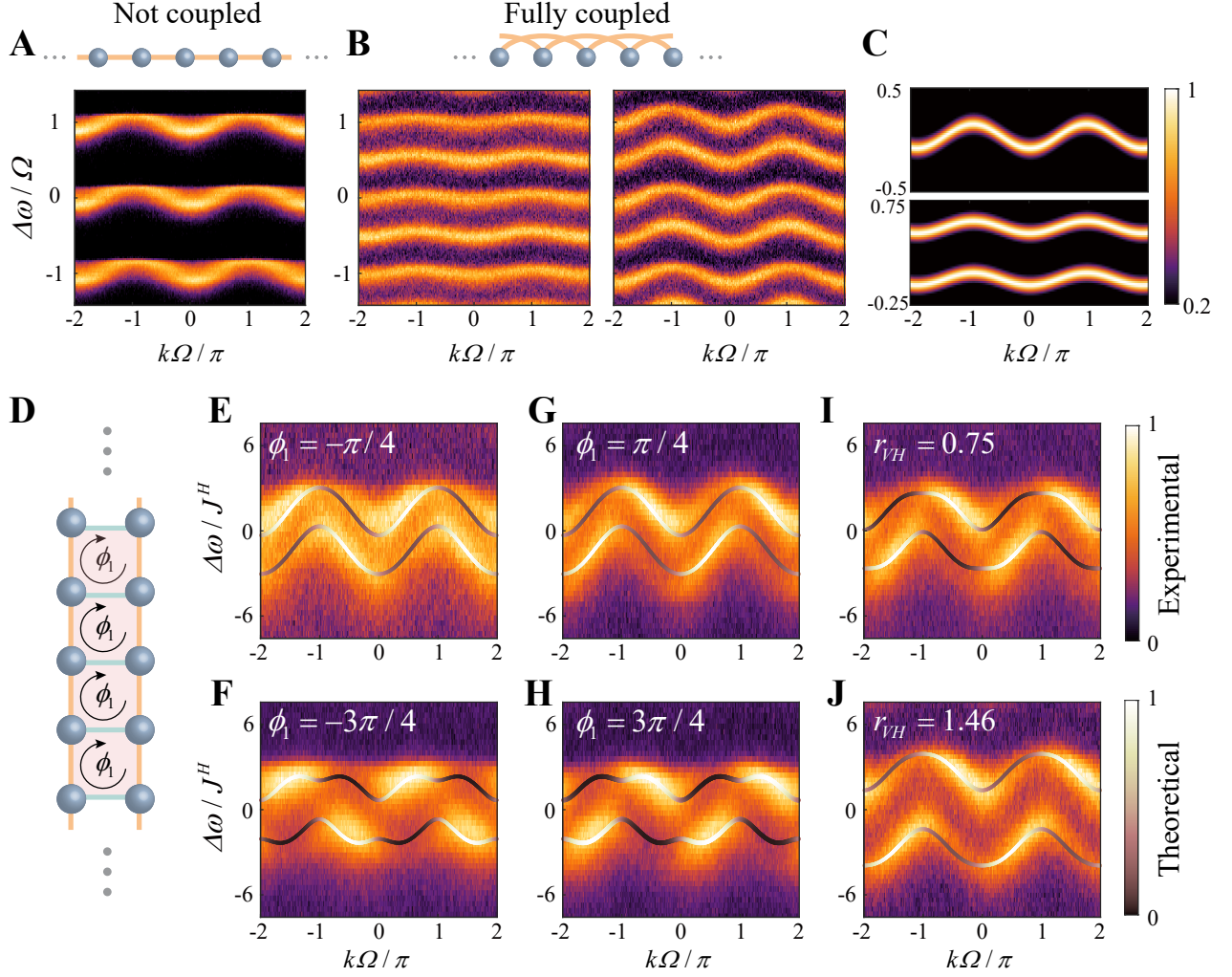


**Fig. 2. Experimental obtained band structures of tight-binding lattices and the Hall ladder.** The band structures exhibit tight-binding lattice characters when two resonators are either not coupled (A) or fully coupled (B).  $J_B^H$  is set to zero in the left plot of (B), while being equal to  $J_A^H$  in the right plot which consequently doubles the coupling strength. (C) The upper and the lower plots are respectively the numerical calculations of (A) and the left plot of (B), using a photonic integrated circuit design software. (D) Illustration of the Hall ladder where the crossing coupling is absent. (E to H) The heat maps are the experimentally obtained band structures of the Hall ladder with coupling strength ratio  $r_{VH} = J_V/2J_H = 0.75$ ,  $J^H = 0.06\Omega$  and an effective magnetic flux  $\phi_1$  being  $\pm\pi/4$  or  $\pm 3\pi/4$ . The lines on them are the corresponding theoretical bands solved from the  $k$ -space Hamiltonian. The distribution information on the two spins (resonators) are encoded in the normalized intensities of both the experimental and theoretical normalized intensities, represented by two sets of colors. Choosing opposite fluxes is equivalent to selectively exciting the opposite spin (injecting into the other resonator). For one spin (E and F), the negative (positive)  $k$  states in the first Brillouin zone predominate the upper (lower) bands. Meanwhile, complementary patterns appear in the other spin (G and H), signifying the spin-momentum locking. (I and J) Using  $\phi_1 = \pi/2$  as an example,  $r_{VH}$  is increase from 0.75 to 1.46 and the spin-momentum locking effect is reduced.

coupling phases ( $\phi_{i,p}^H$ ,  $\phi_p^V$ ,  $\phi_{i,p}^C$ ), where  $i$  denotes the  $i$ -th lattice. In the frequency domain, the synthetic lattice points are formed by the resonant modes of each resonator with identical spacing of the free spectral range (FSR)  $\Omega$ . The phase modulation on the resonators with frequency equal to  $p\Omega$  couples the  $n$ -th and  $(n+p)$ -th lattice points of each lattice (resonator), signifying the horizontal coupling. The vertical coupling indicates

the interaction purely in the spatial domain, i.e., the coupling between the nearest inter-lattice points of the adjacent lattices, which was commonly achieved by a beam splitter with a fixed splitting ratio. To promote convenience and versatility, we replace the splitter with a electro-optic tunable  $2 \times 2$  MZI (Fig. 1A). As the splitting ratio of the MZI can be continuously tuned from zero to unity with a direct-current (DC) voltage, the lattices can



be arbitrarily adjusted from being completely uncoupled to being fully coupled into a lattice with spacing  $\Omega/2$ . This advantage can particularly benefit the applications where fine coupling-strength tuning are required, e.g., simulating and extracting Zak phase of SSH model.

Moreover, we highlight that this design makes it possible to deflect the interaction along the spatial direction towards the frequency direction. To be concrete, by adding modulation of frequency  $p\Omega$  on the MZI other than the resonators, the mode hops  $p$  sites along the frequency direction while crossing to the adjacent resonators, which manifests the cross coupling is satisfied. The introducing of long-range interaction between lattices remarkably raise the complexity of the model and provide opportunity to directly modify the off-diagonal elements of the Hamiltonian matrix in the quasi-momentum space.

Without losing generality, we show experimental demonstration of the fundamental ingredient of the network — the two-resonator protocols in the following. We denote the resonators by A and B, respectively. Retaining the nearest neighbouring coupling in the horizontal and crossing coupling ( $p = 1$ ) and setting  $\phi^V$  to zero, the model turns into the Creutz ladder. We show its schematic in Fig. 1B, of which the Hamiltonian reads

$$H = - \sum_n (J_A^H e^{-i\phi_A^H} a_{n+1}^\dagger a_n + J_B^H e^{-i\phi_B^H} b_{n+1}^\dagger b_n) - \sum_n J^V b_n^\dagger a_n - \sum_n J^C e^{-i\phi^C} (a_{n+1}^\dagger b_n + b_{n+1}^\dagger a_n) + h.c., \quad (1)$$

with  $h.c.$  representing the Hermitian conjugate.

## Experiment

The experimental setup is illustrated in Fig. 1C. On a TFLN platform, we design and fabricate the double resonators coupled by a MZI with three sets of electrodes. The DC signal applied on the resonators through the Bias-Tees is to align their resonant frequencies. Given the reciprocal relationship between the time domain and the frequency domain, time can be considered as the quasi-momentum ( $k$ ) associated with the frequency lattice. We obtain the  $k$ -space band structures with the time-resolved spectroscopy approach that is proposed in Ref. [17] exploiting Floquet theory and beyond rotating-wave approximation. Adjusting the detuning  $\Delta\omega$  of the probe laser injected into resonator A, we can selectively excite different slices of the band structures. The data is collected from the drop port of the same resonator, which leads to the projection of the band structures on the lattice A. The temporal data for each excited slice allows us to reconstruct the entire projected band structure through data stacking. The intensities of the patterns are proportional to the square of the distribution on lattice A [45]. Additionally, a piezoelectric driven Fabry-Perot cavity is employed as an optical spectrum analyzer to filter specific frequency components within the temporal data, enabling a detailed analysis of the

mode distribution.

## Tight-binding single lattice and Hall ladder

We start from applying local modulation on the resonators and only DC signals on the MZI ( $J^C = 0$ ), reducing the Creutz ladder to the Hall ladder. Specially, when the MZI is tuned to disconnect two resonators or to fully couple them, the model further reduces to a tight-binding single lattice.

In Fig. 2A and B, we present the experimentally observed sinusoidal band structures of the tight-binding single lattices. On one hand, when the resonators are not coupled, the lattice constant is  $\Omega$  and the nearest-neighbouring lattice points are coupled. On the other hand, when the resonators are fully coupled, the lattice constant is halved and only the next-near-neighbouring lattice points are coupled, doubling the bands. The splitting ratio of the beam splitters in the MZI exhibit a slight deviation from equal division, resulting in imperfections in the experimental outcomes.

Fig. 2E-J illustrates the projected band structures of the Hall ladder with various synthetic magnetic flux  $\phi_1 = 2\phi_A^H = -2\phi_B^H$  that indicates potential gauges. As the two resonators can be alternatively depicted as pseudospins ( $n_+$ ,  $n_-$ ), the Hall ladder can signify spin-orbit coupling controlled by the magnetic field. Let  $J^H = J_A^H = J_B^H$  and with the proper choice of  $\phi_1$ , we observe a pronounced dependence of the pseudospin character on  $k$ . The probe laser selectively excites the band associated with pseudospin  $n_+$ , represented by the incident resonator A (Fig. 2E and F). In the first Brillouin zone, for  $k > 0$ , the excitation occurs in the upper branch, whereas for  $k < 0$ , it occurs in the lower branch. Upon inverting the magnetic flux to  $-\phi_1$ , resonator A turns into pseudospin  $n_-$  due to symmetry. Consequently, the band structures exhibit mirrored patterns, indicative of chiral spin-momentum locking. Notably, we observe a weakening of this locking effect when the ratio  $J^H/J^V$  decreases as illustrated in Fig. 2I and J.

## Creutz ladder

Compared to the two-leg Hall ladder, the full Creutz ladder enables cross coupling between the two lattices, introduces an extra tunable magnetic flux  $\phi_2$  and  $\phi_3$ , and provides feasibility to combine band flatness and topology. In a similar manner, the cross coupling strength is tuned by the sinusoidal RF signal amplitude and the magnetic flux is modified by the relative phases between three driving signals.

We again set equal coupling strength within each lattice and  $\phi_2 = -\phi_3 = \phi^C - \phi_A^H$ . In Fig. 3A-E, we activate all three types of couplings and alter magnetic flux to experimentally obtain band structures, which are in excellent agreement with the theoretical prediction. To experimentally obtain band flatness, we adjust the DC signal to neutralize the second type of coupling  $J^V$  and then set  $J^C = J^H$ ,  $\phi_A^H = -\phi_B^H = \pi/2$  and  $\phi^C = 0$ . The obtained flat band is displayed in Fig. 3F. The Aharonov-Bohm cage effect is one of the direct topological features of the Creutz ladder under the flatness condition, where



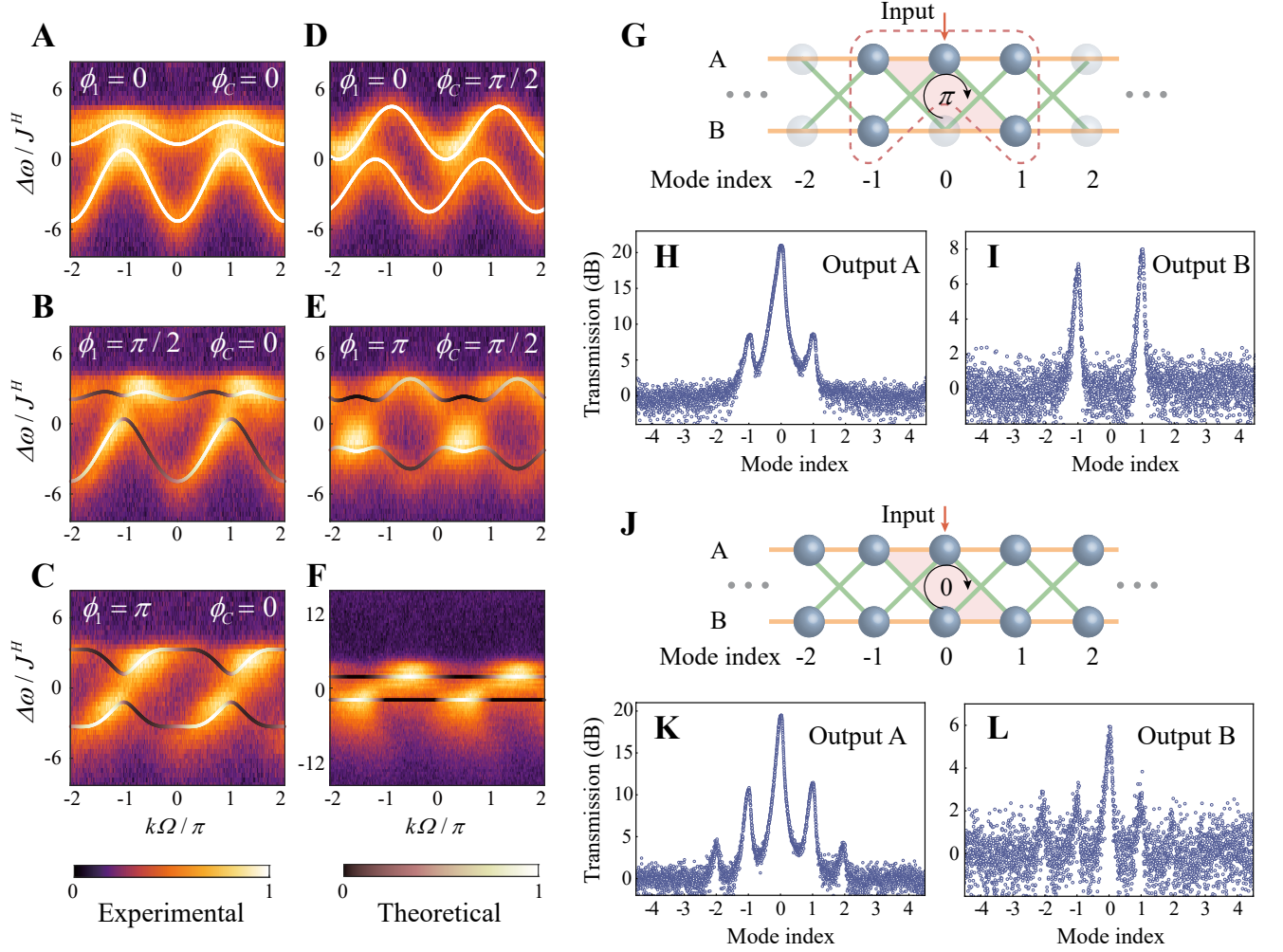


Fig. 3. **Experimental obtained band structures of the Creutz ladder and direct observation of the Aharonov-Bohm cage effect.** (A to E) The heat maps display the general band structures of the Creutz ladder given different  $\phi_1$  and  $\phi_D$ , where  $J^V/2J^H = 1.1$ ,  $J^C/J^H = 0.52$  and  $J^H = 0.06\Omega$ . (F) The flat band structure measured at  $J^V = 0$ ,  $J^H = J^C$ ,  $J^H = 0.028\Omega$  and  $\phi_A^H = -\phi_B^H = \pi/2$  when the Aharonov-Bohm cage effect occurs. The lines on the experimental results are the corresponding theoretical bands solved from the  $k$ -space Hamiltonian. The distribution information on the two spins (resonators) are encoded in the normalized intensities of both the experimental and theoretical normalized intensities, represented by two sets of colors. (G) Illustration of the Aharonov-Bohm cage effect where the phase collected in a round trip in the pink area is  $\pi$ . When a probe light is input from resonator A with frequency near the zero index mode, the distribution is caged within the dashed box ( $0, \pm 1$  in lattice A and  $\pm 1$  in lattice B). (H and I) The experimental readout of the mode distribution from the drop ports of resonator A and B measured by a Fabry-Perot cavity. The distribution other than those inside the dashed box is clearly suppressed. (J) Illustration of the not caged situation where the phase collected in the pink area is zero. The light normally spreads out along the frequency direction. (K and L) The experimental results of the not caged situation, where more modes survives compared to the caged ones. The distribution results are plotted in the logarithmic coordinates.

the wave function is caged within five sites although no boundary on lattices is introduced (Fig. 3G). To directly observe the clues of the Aharonov-Bohm cage effect, in the same situation of Fig. 3F, we inject the laser near the center (zeroth) frequency into resonator A and detect the mode distribution from the drop ports of resonator A and B by a scanning Fabry-Perot cavity. We note that the caging effect is not sensitive to the input laser frequency and we set the laser detuning to approximate  $2J^H$  for highest signal intensity. More information can be found

in Supplementary Materials. Aside from the flat band in the  $k$  space, we also observe the cage effect in the real (frequency) space and the experimental results are shown in Fig. 3H and I. The distribution on the zeroth site of lattice B and high order sites (absolute value larger than one) of both lattices are clearly suppressed, featuring the caging effect. As comparison, the experimental results of the not-caged situation where  $\phi_A^H = \phi_B^H = 0$  (Fig. 3J) is displayed in Fig. 3K and L.

## Discussion

In conclusion, we design a MZI-assisted double-resonator device and experimentally demonstrate its versatility and flexibility by arbitrarily tuning the MZI with DC and RF signals. The device makes better use of the interplay of the frequency and spatial domain, and covers a vast range of possible coupling in the mentioned parameters that can be finely modified in principle. We witness the important phenomena manifesting topology of the famous Hall ladder and Creutz ladder including the band structures modified by different synthetic magnetic fields, spin-momentum locking and Aharonov-Bohm cage effect, which paves the way for simulating more complex physical models and even predicting novel phenomena. The Aharonov-Bohm cage effect may also be utilized for engineering the number of the side bands or frequency shifting.

Therefore, our design holds significant potential in building large and high-dimensional networks as both the spatial and frequency domain can be expanded to a larger scale and a higher dimension. This makes it particularly suitable for realization on integrated optics for its striking merits such as high scalability and stability. Moreover, the TFLN is an excellent platform that not only possesses these advantages, but also has high non-linear and electric-optic coefficients, which is well-suited for our approach. However, the realization may also face challenges, for example, multiple modulation on one resonator requires long modulation area which may conflict with the requirement of loss and influence the results. Despite of this, processing on TFLN is developing rapidly recently and the performance of elements has been raising, such as less propagation loss and insertion loss and increasing the precision of the beam splitter. Hence, we believe these challenges can be addressed in the near future and our work may shed light on more interesting exploration on synthetic dimensions.

## Methods

Our device was fabricated on an x-cut lithium niobate on insulator wafer from NANOLN, where the 400-nm

lithium niobate film and a 4.7- $\mu\text{m}$   $\text{SiO}_2$  layer are on a 525- $\mu\text{m}$  Si substrate in order. The resonators were patterned on a Hydrogen silsesquioxane (HSQ) film with electron-beam lithography (EBL). Subsequently, 200-nm lithium niobate was etched out via an  $\text{Ar}^+$ -based inductively coupled plasma etching (ICP-RIE) process. The residual HSQ and the redeposition were removed by a wet etching process. Two layers of ultraviolet photoresist LOR5A and S1813 were spin-coated on the device and the “bridges” for electrodes to cross the waveguides were defined by markless lithography. Then 750-nm  $\text{SiO}_2$  was deposited and followed by a lift-off process. Subsequently, 800-nm copper electrodes were plated with a similar process. Finally, the electrodes were connected to a high-frequency printed circuit board (PCB) with bonding wires. The FSR of the resonators are approximate  $\Omega = 2\pi \times 8.9$  GHz. The loaded Q-factor before plating electrodes was  $3.7 \times 10^5$ , while after plating the load Q-factor decreased to  $1.7 \times 10^5$  due to metal absorption. More details can be found in Supplementary information.

The RF signals were produced by three tunable microwave sources (AnaPico APUASYN20) and amplified by three amplifiers (Minicircuit ZVE-3W-183+). A distributed feedback laser is injected to the device after a polarization controller through grating couplers. The output signals are collected and analyzed by either a fast oscilloscope (Keysight DCA-X 86100D) or a Fabry-Perot cavity of which the mirror reflectivity is 98% and the cavity length is approximate 1.5 millimeter.

## Acknowledgements

This work is supported by the Innovation Program for Quantum Science and Technology (No. 2021ZD0301200), the National Natural Science Foundation of China (No. 12174370, 12174376, and 11821404, 12304546), the Youth Innovation Promotion Association of Chinese Academy of Sciences (No. 2017492), Anhui Provincial Natural Science Foundation (No. 2308085QA28), China Postdoctoral Science Foundation (No. 2023M733412). This work was partially carried out at the USTC Center for Micro and Nanoscale Research and Fabrication.

- 
- [1] E. Lustig, S. Weimann, Y. Plotnik, Y. Lumer, M. A. Bandres, A. Szameit, and M. Segev, Photonic topological insulator in synthetic dimensions, *Nature* **567**, 356 (2019).
  - [2] T. Ozawa, H. M. Price, A. Amo, N. Goldman, M. Hafezi, L. Lu, M. C. Rechtsman, D. Schuster, J. Simon, O. Zilberberg, *et al.*, Topological photonics, *Rev. Mod. Phys.* **91**, 015006 (2019).
  - [3] L. Lu, J. D. Joannopoulos, and M. Soljačić, Topological photonics, *Nat. Photonics* **8**, 821 (2014).
  - [4] S. K. Sridhar, S. Ghosh, D. Srinivasan, A. R. Miller, and A. Dutt, Quantized topological pumping in floquet synthetic dimensions with a driven dissipative photonic molecule, *Nature Physics*, **1** (2024).
  - [5] A. Regensburger, C. Bersch, M.-A. Miri, G. Onishchukov, D. N. Christodoulides, and U. Peschel, Parity-time synthetic photonic lattices, *Nature* **488**, 167 (2012).
  - [6] X.-W. Luo, X. Zhou, C.-F. Li, J.-S. Xu, G.-C. Guo, and Z.-W. Zhou, Quantum simulation of 2d topological physics in a 1d array of optical cavities, *Nat. Commun.* **6**, 7704 (2015).
  - [7] X.-W. Luo, X. Zhou, J.-S. Xu, C.-F. Li, G.-C. Guo, C. Zhang, and Z.-W. Zhou, Synthetic-lattice enabled all-optical devices based on orbital angular momentum of light, *Nat. Commun.* **8**, 16097 (2017).
  - [8] L. Yuan, Q. Lin, M. Xiao, and S. Fan, Synthetic dimension in photonics, *Optica* **5**, 1396 (2018).
  - [9] L. Yuan, Q. Lin, A. Zhang, M. Xiao, X. Chen, and S. Fan, Photonic gauge potential in one cavity with synthetic frequency and orbital angular momentum dimensions, *Phys. Rev. Lett.* **122**, 083903 (2019).
  - [10] L. Yuan, A. Dutt, and S. Fan, Synthetic frequency

- dimensions in dynamically modulated ring resonators, *APL Photonics* **6**, 071102 (2021).
- [11] L. Yuan, M. Xiao, Q. Lin, and S. Fan, Synthetic space with arbitrary dimensions in a few rings undergoing dynamic modulation, *Phys. Rev. B* **97**, 104105 (2018).
  - [12] K. Fang, Z. Yu, and S. Fan, Realizing effective magnetic field for photons by controlling the phase of dynamic modulation, *Nat. Photonics* **6**, 782 (2012).
  - [13] Y. Lumer, M. A. Bandres, M. Heinrich, L. J. Maczewsky, H. Herzig-Sheinfux, A. Szameit, and M. Segev, Light guiding by artificial gauge fields, *Nat. Photonics* **13**, 339 (2019).
  - [14] K. Wang, B. A. Bell, A. S. Solntsev, D. N. Neshev, B. J. Eggleton, and A. A. Sukhorukov, Multidimensional synthetic chiral-tube lattices via nonlinear frequency conversion, *Light: Sci. Appl.* **9**, 132 (2020).
  - [15] Y. Chen, Y.-L. Zhang, Z. Shen, C.-L. Zou, G.-C. Guo, and C.-H. Dong, Synthetic gauge fields in a single optomechanical resonator, *Phys. Rev. Lett.* **126**, 123603 (2021).
  - [16] G. Li, L. Wang, R. Ye, Y. Zheng, D.-W. Wang, X.-J. Liu, A. Dutt, L. Yuan, and X. Chen, Direct extraction of topological zak phase with the synthetic dimension, *Light: Sci. Appl.* **12**, 81 (2023).
  - [17] A. Dutt, M. Minkov, Q. Lin, L. Yuan, D. A. B. Miller, and S. Fan, Experimental band structure spectroscopy along a synthetic dimension, *Nat. Commun.* **10**, 3122 (2019).
  - [18] A. Dutt, Q. Lin, L. Yuan, M. Minkov, M. Xiao, and S. Fan, A single photonic cavity with two independent physical synthetic dimensions, *Science* **367**, 59 (2020).
  - [19] A. Dutt, L. Yuan, K. Y. Yang, K. Wang, S. Buddhiraju, J. Vučković, and S. Fan, Creating boundaries along a synthetic frequency dimension, *Nat. Commun.* **13**, 3377 (2022).
  - [20] G. Li, Y. Zheng, A. Dutt, D. Yu, Q. Shan, S. Liu, L. Yuan, S. Fan, and X. Chen, Dynamic band structure measurement in the synthetic space, *Sci. Adv.* **7**, eabe4335 (2021).
  - [21] K. Wang, A. Dutt, K. Y. Yang, C. C. Wojcik, J. Vuckovic, and S. Fan, Generating arbitrary topological windings of a non-hermitian band, *Science* **371**, 1240 (2021).
  - [22] K. Wang, A. Dutt, C. C. Wojcik, and S. Fan, Topological complex-energy braiding of non-hermitian bands, *Nature* **598**, 59 (2021).
  - [23] M. Zhang, C. Wang, P. Kharel, D. Zhu, and M. Lončar, Integrated lithium niobate electro-optic modulators: when performance meets scalability, *Optica* **8**, 652 (2021).
  - [24] J. Lin, F. Bo, Y. Cheng, and J. Xu, Advances in on-chip photonic devices based on lithium niobate on insulator, *Photon. Res.* **8**, 1910 (2020).
  - [25] M. Zhang, B. Buscaino, C. Wang, A. Shams-Ansari, C. Reimer, R. Zhu, J. M. Kahn, and M. Lončar, Broadband electro-optic frequency comb generation in a lithium niobate microring resonator, *Nature* **568**, 373 (2019).
  - [26] M. Zhang, C. Wang, R. Cheng, A. Shams-Ansari, and M. Lončar, Monolithic ultra-high-q lithium niobate microring resonator, *Optica* **4**, 1536 (2017).
  - [27] H. Feng, T. Ge, X. Guo, B. Wang, Y. Zhang, Z. Chen, S. Zhu, K. Zhang, W. Sun, C. Huang, *et al.*, Integrated lithium niobate microwave photonic processing engine, *Nature* **627**, 80 (2024).
  - [28] M. Yu, D. Barton III, R. Cheng, C. Reimer, P. Kharel, L. He, L. Shao, D. Zhu, Y. Hu, H. R. Grant, *et al.*, Integrated femtosecond pulse generator on thin-film lithium niobate, *Nature* **612**, 252 (2022).
  - [29] M. Xu, M. He, H. Zhang, J. Jian, Y. Pan, X. Liu, L. Chen, X. Meng, H. Chen, Z. Li, *et al.*, High-performance coherent optical modulators based on thin-film lithium niobate platform, *Nat. Commun.* **11**, 3911 (2020).
  - [30] T. Ozawa, H. M. Price, N. Goldman, O. Zilberberg, and I. Carusotto, Synthetic dimensions in integrated photonics: From optical isolation to four-dimensional quantum hall physics, *Phys. Rev. A* **93**, 043827 (2016).
  - [31] G. Li, L. Wang, R. Ye, S. Liu, Y. Zheng, L. Yuan, and X. Chen, Observation of flat-band and band transition in the synthetic space, *Advanced Photonics* **4**, 036002 (2022).
  - [32] H. X. Dinh, A. Balčytis, T. Ozawa, Y. Ota, G. Ren, T. Baba, S. Iwamoto, A. Mitchell, and T. G. Nguyen, Reconfigurable synthetic dimension frequency lattices in an integrated lithium niobate ring cavity, *Commun. Phys.* **7**, 185 (2024).
  - [33] R. Ye, G. Li, S. Wan, X. Xue, P. Wang, X. Qiao, H. Li, S. Liu, J. Wang, R. Ma, *et al.*, Construction of various time-dependent hamiltonians on a single photonic chip, *arXiv:2408.00287* (2024).
  - [34] U. A. Javid, R. Lopez-Rios, J. Ling, A. Graf, J. Staffa, and Q. Lin, Chip-scale simulations in a quantum-correlated synthetic space, *Nat. Photonics* **17**, 883 (2023).
  - [35] Y. Hu, C. Reimer, A. Shams-Ansari, M. Zhang, and M. Loncar, Realization of high-dimensional frequency crystals in electro-optic microcombs, *Optica* **7**, 1189 (2020).
  - [36] Y. Hu, M. Yu, N. Sinclair, D. Zhu, R. Cheng, C. Wang, and M. Lončar, Mirror-induced reflection in the frequency domain, *Nat. Commun.* **13**, 6293 (2022).
  - [37] Z.-A. Wang, Y.-T. Wang, X.-D. Zeng, J.-M. Ren, W. Liu, X.-H. Wei, Z.-P. Li, Y.-Z. Yang, N.-J. Guo, L.-K. Xie, J.-Y. Liu, Y.-H. Ma, J.-S. Tang, Z.-W. Zhou, C.-F. Li, and G.-C. Guo, On-chip photonic simulating band structures towards arbitrary-range coupled frequency lattices, to appear at *Phys. Rev. Lett.*
  - [38] M. Creutz, End states, ladder compounds, and domain-wall fermions, *Phys. Rev. Lett.* **83**, 2636 (1999).
  - [39] J. Zurita, C. E. Creffield, and G. Platero, Topology and interactions in the photonic creutz and creutz-hubbard ladders, *Advanced Quantum Technologies* **3**, 1900105 (2020).
  - [40] J. S. C. Hung, J. H. Busnaina, C. W. S. Chang, A. M. Vadiraj, I. Nsanzineza, E. Solano, H. Alaeian, E. Rico, and C. M. Wilson, Quantum simulation of the bosonic creutz ladder with a parametric cavity, *Phys. Rev. Lett.* **127**, 100503 (2021).
  - [41] Y. He, R. Mao, H. Cai, J.-X. Zhang, Y. Li, L. Yuan, S.-Y. Zhu, and D.-W. Wang, Flat-band localization in creutz superradiance lattices, *Phys. Rev. Lett.* **126**, 103601 (2021).
  - [42] T. Dai, A. Ma, J. Mao, Y. Ao, X. Jia, Y. Zheng, C. Zhai, Y. Yang, Z. Li, B. Tang, *et al.*, A programmable topological photonic chip, *Nature Materials* , 1 (2024).
  - [43] L. Yuan, M. Xiao, Q. Lin, and S. Fan, Synthetic space with arbitrary dimensions in a few rings undergoing dynamic modulation, *Phys. Rev. B* **97**, 104105 (2018).



- [44] Q. Lin, X.-Q. Sun, M. Xiao, S.-C. Zhang, and S. Fan, A three-dimensional photonic topological insulator using a two-dimensional ring resonator lattice with a synthetic frequency dimension, [Sci. Adv. 4, eaat2774 \(2018\)](#).
- [45] See Supplementary Information for more details.